Journal of Colloid and Interface Science 648 (2023) 406–417

Contents lists available at ScienceDirect

Journal of Colloid And Interface Science

journal homepage: www.elsevier.com/locate/jcis

Firmly interlocked Janus-type metallic $Ni_3Sn_2S_2$-carbon nanotube heterostructure suppresses polysulfide dissolution and Sn aggregation

Niloofar Kolivand [a,1], Safa Haghighat-Shishavan [b,1], Mahboobeh Nazarian-Samani [b], Mehdi Kheradmandfard [a], Masoud Nazarian-Samani [b,*], Seyed Farshid Kashani-Bozorg [a,*], Wooyoung Lee [b,*]

[a] School of Metallurgy and Materials Engineering, College of Engineering, University of Tehran, Tehran 11155-4563, Iran
[b] Department of Materials Science and Engineering, Yonsei University, 50 Yonsei-ro, Seodaemun-gu, Seoul 03722, Republic of Korea

GRAPHICAL ABSTRACT

Janus-type $Ni_3Sn_2S_2$-CNT heterostructure can efficiently tolerate the large volume expansions of electrode materials, prevent their detrimental aggregation, barricade the oxidation and shuttling of intermediate polysulfides, and guarantee reversible redox reactions for durable cycles.

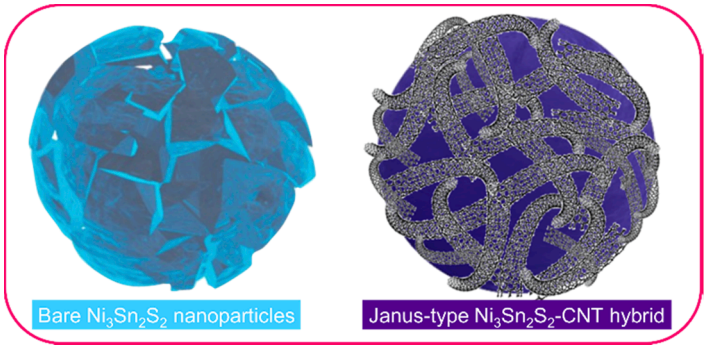

ARTICLE INFO

Keywords:
$Ni_3Sn_2S_2$
Janus
Shuttle effect
Aggregation
Li-ion batteries
Solid-electrolyte interphase

ABSTRACT

Ternary transition-metal tin chalcogenides, with their diverse compositions, abundant constituents, high theoretical capacities, acceptable working potentials, excellent conductivities, and synergistic active/inactive multicomponents, hold promise as anode materials for metal-ion batteries. However, abnormal aggregation of Sn nanocrystals and the shuttling of intermediate polysulfides during electrochemical tests detrimentally affect the reversibility of redox reactions and lead to rapid capacity fading within a limited number of cycles. In this study, we present the development of a robust Janus-type metallic $Ni_3Sn_2S_2$-carbon nanotube (NSSC) heterostructured anode for Li-ion batteries (LIBs). The synergistic effects of $Ni_3Sn_2S_2$ nanoparticles and a carbon network successfully generate abundant heterointerfaces with steady chemical bridges, thereby enhancing ion and electron transport, preventing the aggregation of Ni and Sn nanoparticles, mitigating the oxidation and shuttling of polysulfides, facilitating the reforming of $Ni_3Sn_2S_2$ nanocrystals during delithiation, creating a uniform solid-electrolyte interphase (SEI) layer, protecting the mechanical integrity of electrode materials, and ultimately

* Corresponding authors.
E-mail addresses: masoud.nazarian@gmail.com (M. Nazarian-Samani), fkashani@ut.ac.ir (S.F. Kashani-Bozorg), wooyoung@yonsei.ac.kr (W. Lee).
[1] These authors contributed equally to this work.

https://doi.org/10.1016/j.jcis.2023.05.176
Received 8 February 2023; Received in revised form 19 May 2023; Accepted 28 May 2023
Available online 1 June 2023

enabling highly reversible lithium storage. Consequently, the NSSC hybrid exhibits an excellent initial Coulombic efficiency (ICE > 83 %) and superb cyclic performance (1218 mAh/g after 500 cycles at 0.2 A/g and 752 mAh/g after 1050 cycles at 1 A/g). This research provides practical solutions for the intrinsic challenges associated with multi-component alloying and conversion-type electrode materials in next-generation metal-ion batteries.

1. Introduction

To expedite the progress and commercialization of LIBs, it is urgent to explore innovative, high-performance anode materials with high theoretical capacities, safe working potentials, appropriate structural stability, abundant components, and quick Li^+-diffusion kinetics, as compared to traditional graphite anodes [1–3]. It has been demonstrated that many alloying- and/or conversion-type anodes, based on abundant Si, Ge, Sn, Al, P, S, and Se in their elemental or compound-structured states, properly meet the requirements for high capacity and suitable operating potentials for durable Li storage. However, they still suffer from poor reversibility and structural integrity. Moreover, some of these elements have additional intrinsic problems that need to be addressed with extra strategies in order to realize high-performance alloying-/conversion-based anodes. For example, Sn inherently suffers from abnormal grain growth and uncontrollable aggregation during initial cycles in different metal-ion batteries [4–8]. In terms of S-rich anodes, they extensively suffer from sluggish kinetics of conversion reactions during the formation/decomposition of Li_2S. Additionally, intermediate soluble lithium polysulfides tend to dissolve into the electrolyte, causing electrolyte deterioration and rapid capacity fading [9–12].

Ternary stoichiometric shandite-type chalcogenides with a general formula of $A_3M_2Ch_2$ (A = Co, Ni, Rh, Pd; M = Sn, In, Pb, Tl; Ch = S, Se) and a general space group of $R\bar{3}m$ have recently attracted extensive attention due to their remarkable thermoelectric, magnetic, superconducting, catalytic, optical, and electronic applications [13–19]. Ternary nickel tin chalcogenide (also known as nickel tin sulfide: $Ni_3Sn_2S_2$) is an excellent representative of this extensive family. It is considered a promising candidate for LIB anodes primarily because of its metallic nature, superb electronic conductivity, excellent structural and chemical stability, and high theoretical capacity (718 mAh/g) resulting from the formation of Li_2S and $Li_{22}Sn_5$ discharge products. Furthermore, the high Ni content provides excellent buffering effects to mitigate the significant volume expansions during electrochemical tests. Additionally, Ni enhances the electrical conductivity and Li^+ diffusion, promotes redox reactions during cycling tests, and inhibits the coarsening/aggregation of Sn and the shuttling of polysulfides [20–23]. However, to the best of the authors' knowledge, the electrochemical performance of $Ni_3Sn_2S_2$ as an anode in LIBs has not been investigated to date [24–26].

Moreover, it has been widely demonstrated that designing sophisticated heterostructures with abundant heterointerfaces is substantially required to solve the problems of electrode materials for long-term electrochemical tests [3,27–29]. Various carbon structures are suitable for synergistically building strong, permanent chemical connections between two components, preserving the structural integrity of active materials during charging/discharging, promoting the transport of electrons and Li^+ ions, preventing excessive contact between the electrolyte and electrode materials, generating a stable SEI film, and ultimately suppressing the intrinsic challenges of Sn and S for long-term cycles [4,30]. In addition, multi-component discharging/recharging products formed at various potentials, along with tiny Ni nanoparticles, may act as buffering agents to reasonably alleviate volume change, polysulfide shuttling, and Sn aggregation [4,31,32].

This study proposes an innovative Janus-type NSSC heterostructure with robust chemical bonds between the $Ni_3Sn_2S_2$ (NSS) nanoparticles and carbon network to address the issues of Sn aggregation, polysulfide shuttling, and quick capacity fading of Sn- and S-rich anodes in LIBs. This is achieved through the benefits of chemical coupling, a protective carbon nanotube (CNT) network, and tiny Ni nanocrystals. Compared to other heterostructured anodes, this binary hybrid exhibits a "Janus interfacial effect" with unique interfacial coupling states, thereby enhancing electrostatic adsorption, charge/mass transport, and likely active ion storage locations [33–39]. In this binary Janus-type heterostructure, both the $Ni_3Sn_2S_2$ nanoparticles and multi-walled CNT network have metallic characteristics and synergistically provide superb electrical conductivity to the entire electrode. Moreover, $Ni_3Sn_2S_2$ functions as the main active component for reversible ion storage, while the CNT network independently serves as a uniform, steady matrix to prevent the aggregation and coarsening of Sn nanocrystals, maintain the structural integrity of the hybrid, trap intermediate polysulfides, and enhance surface pseudocapacitive ion storage. Consequently, this high-performance Janus-type heterostructure leads to the formation of a thin SEI layer and the persistent formation of discharge products (Li_2S, Li_2O, and $Li_{22}Sn_5$). As a result, the NSSC Janus-type hybrid exhibits outstanding ICE and excellent cycling performance for>1000 cycles at high current rates.

2. Results and discussion

As depicted in Fig. S1a, $Ni_3Sn_2S_2$ exhibits a trigonal crystallographic structure belonging to the $R\bar{3}m$ space group. The electron localization function (ELF) images of the $Ni_3Sn_2S_2$ structure in different (0 0 1), (1 1 1), and ($\bar{1}\bar{1}$0) planes (Fig. S1b) reveal that the Ni and Sn atomic positions display perfect electronic charge localizations (blue areas, equivalent to 1.0 e/bohr^3), while the S sites exhibit weak charge localizations. Consequently, the presence of two metallic Ni and Sn atomic positions generates regions with intermediate electronic localization (green regions with 0.5 e/bohr^3), where a large number of free gas-like electrons exist, greatly enhancing electron transport and conductivity [40,41]. Importantly, Fig. 1a illustrates that $Ni_3Sn_2S_2$ possesses a zero bandgap energy, indicating its semi-metallic nature and excellent electrical conductivity, which contribute to the improved electrochemical tests.

NSS nanoparticles were synthesized efficiently in a time-effective manner using a convenient microwave irradiation approach. Diethylene glycol (DEG), acting as an efficient solvent, played a crucial role in the formation of agglomeration-free nanoparticles. This was mainly due to its copious hydroxyl functional groups and high viscosity. DEG successfully formed complexes with nonmetal/metal ions and hindered their rapid transfer in the solvent [42]. Consequently, when sodium borohydride ($NaBH_4$) was added as a reducing agent to the homogeneous mixture of precursors and solvent, the nonmetal/metal ions were unable to move rapidly and were compelled to promptly generate a well-dispersed, reduced Ni-Sn-S precursor. Eventually, after only 8 min of microwave irradiation, uniform NSS nanoparticles were formed. H_2 gas bubbles released from the $NaBH_4$ were continuously dispersed into the solution during microwave heating, facilitating the concurrent reduction process and in situ phase transformation without any undesirable aggregation or clustering [43–47].

Fig. S2a presents the transmission electron microscopy (TEM) image of NSS powders, displaying an interconnected semi-spherical morphology with an even particle size of approximately 50 nm. The high-resolution TEM (HRTEM) image (Fig. S2b) confirmed the crystalline nature of the powders, as lattice fringes attributed to the (1 0 4), (0 1 2), (0 2 1), and (1 1 0) crystallographic planes of $Ni_3Sn_2S_2$ were clearly observed. Further evidence was obtained from the selected area electron diffraction (SAED) and high-resolution X-ray diffraction (XRD)

patterns (Fig. S2c and 1b), which exhibited distinct spots/rings and diffraction peaks that matched ICDD Card No. 00–026-1290, without any presence of unwanted phases or contaminants. TEM images of the NSSC heterostructure are shown in Fig. S2d and e. The morphology of CNTs remained unaltered, and they completely covered the NSS nanoparticles. The corresponding SAED pattern (Fig. S2f) indicated that the crystalline nature of NSS particles remained unchanged after hybrid formation. In addition to the abundant rings and spots in the SAED pattern, two broad rings corresponding to the (0 0 2) and (1 1 0) planes of the carbon framework were observed. High-angle annular dark-field imaging-scanning transmission electron microscopy (HAADF-STEM) images of both the NSS and NSSC powders (Figs. S3 and S4) demonstrated the uniform distribution of Ni, Sn, and S constituents within individual particles and their monotonic embedding within the carbon network, providing evidence of intimate contacts between the nanoparticles and CNTs, constructing a Janus-type hybrid with numerous heterointerfaces.

X-ray photoelectron spectroscopy (XPS) was utilized to analyze the chemical states of individual elements in NSS and NSSC powders and to further explore the chemical bonds between the NSS nanoparticles and the CNT network. Fig. 1c–1f compare the high-resolution Ni 2p, Sn 3d, S 2p, and O 1s XPS spectra of NSS and NSSC samples, respectively. All the spectra in the NSSC heterostructure had lower intensities than those in the bare NSS. Moreover, the peaks were slightly shifted to higher binding energies after hybrid formation, as indicated by arrows in the figures. These two noticeable changes conspicuously demonstrate the strong Ni-O-C, Sn-O-C, and S-O-C chemical bonds between NSS nanocrystals and CNTs [4,30,31,48,49].

In both samples, the high-resolution Ni 2p spectra exhibited two main electronic orbits of Ni $2p_{3/2}$ and Ni $2p_{1/2}$, along with two satellites. Ni $2p_{3/2}$ in NSS was deconvoluted into Ni^{2+} and Ni^{3+} at 855.4 and 856.9 eV, respectively, while Ni $2p_{1/2}$ was divided into the same Ni valence states at 873.2 and 874.6 eV, respectively, and the satellites were located at 861.7 and 879.7 eV [22]. Each Sn 3d spectrum comprised two Sn $3d_{5/2}$ and Sn $3d_{3/2}$ peaks, each of which was deconvoluted into three Sn^0, Sn^{2+}, and Sn^{4+} states, positioned at 485.4, 486.4, and 487.0 eV for Sn $3d_{5/2}$ of NSS, and situated at 493.8, 494.8, and 495.4 eV for Sn $3d_{3/2}$, respectively [22]. The S 2p spectra were deconvoluted into S $2p_{3/2}$, S $2p_{1/2}$, and SO_x, with binding energies for NSS at 162.1, 163.3, and 168.7 eV, respectively [31].

The O 1s spectra mainly originated from oxygen functional groups of CNTs or the superficial oxides formed on the outer sections of nanoparticles during microwave synthesis. The spectra were deconvoluted into three distinct species corresponding to surface chemisorbed oxygen (O-H), oxygen vacancies ($O_{vac.}$), and lattice oxygen (M-O). These components were located at 530.4, 531.3, and 532.0 eV for NSS, respectively.

To evaluate the electrochemical performance of NSS and NSSC, LIB half-cells were assembled using 2032 coin cells and Li counter electrodes. These cells were tested within a voltage range of 0.01–3 V (vs Li^+/Li). Fig. 2a,d displays the CV curves of NSS and NSSC electrodes at a scan rate of 0.05 mV/s. The first reduction scan of NSS exhibited three peaks at 1.69, 1.28, and 0.63 V. In NSSC, these peaks became stronger and slightly shifted to 1.76, 1.34, and 0.66 V, respectively. These peaks are believed to be associated with the conversion reaction of $Ni_3Sn_2S_2$, the construction of the SEI film, and the formation of discharge products (Ni, Li_xSn, and Li_2S) [12,22,50–52]. Additionally, Li_2O was unexpectedly formed as a discharge product. NSSC had another significant peak at approximately 0.01 V due to the irreversible intercalation of Li^+ ions into CNTs. However, this peak progressively weakened in subsequent cycles [53]. Subsequent cathodic scans of both NSS and NSSC electrodes revealed two broad peaks. For bare NSS, these peaks were located at 1.43 and 0.67 V, while for NSSC, they were situated at 1.48 and 0.67 V. The reduction reaction peaks in NSS varied across different cycles, whereas in NSSC, the peaks overlapped each other up to five cycles.

During the first anodic scan of NSS, four broad peaks were observed at 0.52, 1.05, 1.55, and 2.25 V. These peaks were also observed in subsequent cycles, but with weak overlapping. This indicates a weak reversibility of oxidation reactions, large polarization, and fragile structural stability of electrode materials [53]. Conversely, the first oxidation curve of NSSC exhibited several distinct reaction peaks at 0.19, 0.49, 1.02, 1.37, 1.69, and 2.13 V [22,51,52]. These anodic peaks were consistently observed in subsequent cycles. Notably, higher scan rates caused the redox peaks in the bare NSS electrode to fade with negligible areas, whereas the peaks for NSSC remained detectable (Fig. S5).

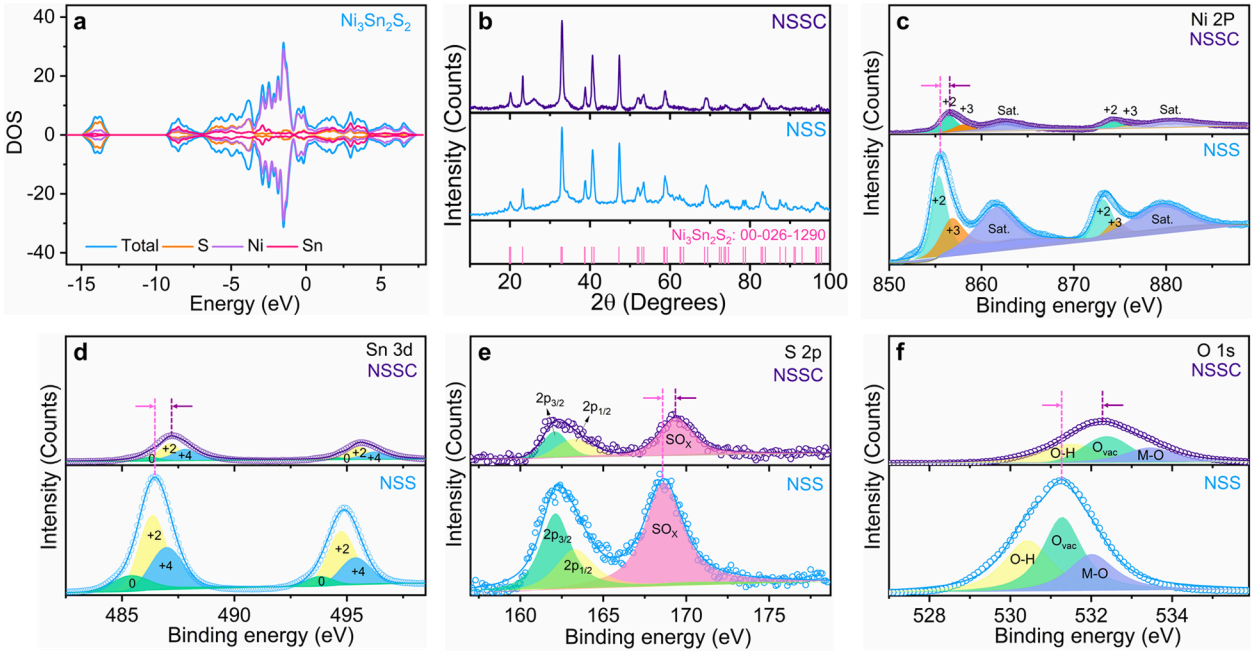

Fig. 1. (a) Total and partial electron density of states of $Ni_3Sn_2S_2$, (b) XRD patterns, and high-resolution (c) Ni 2p, (d) Sn 3d, (e) S 2p, and (f) O 1 s XPS spectra for NSS and NSSC powders.

Fig. 2b and 2e illustrate the galvanostatic charge/discharge profiles of NSS and NSSC electrodes for different cycles at 0.2 A/g, respectively. The initial charge and discharge capacities were 763.1 and 1118.0 mAh/g for the NSS electrode, respectively, equivalent to an ICE of 68.26 %. On the other hand, NSSC delivered 808.9 and 971.0 mAh/g as charge and discharge capacities, corresponding to an ICE of 83.31 %. The charge/discharge profiles of bare NSS also indicated that the capacity rapidly dropped to 130 mAh/g after 60 cycles, whereas the profiles for NSSC remained steady for over 500 cycles. Fig. 2c illustrates the cyclic performance and the representative CE values of the two electrodes at 0.2 A/g. The capacities of NSSC slightly decreased during the initial 25 cycles, beyond which they all increased to approximately 1136 mAh/g after approximately 200 cycles and steadily reached 1218 mAh/g after 500 cycles. The stable SEI layer generation and electrode stabilization are possible reasons for the capacity decline in the primary cycles [54–56]. The rate capability of the two NSS and NSSC electrodes was also probed (Fig. 2f). NSSC delivered 1065, 716, 584, 469, 380, 326, 294, and 249 mAh/g at 0.1, 0.2, 0.5, 0.7, 1, 1.5, 2, and 3 A/g, respectively. The capacities for NSS at 0.1 and 0.2 A/g were slightly higher than those for NSSC (1197 and 750 mAh/g, respectively), beyond which they rapidly declined to 479, 313, 223, 151, 104, and 68 mAh/g at 0.5, 0.7, 1, 1.5, 2, and 3 A/g, respectively. The discharge capacities of NSS and NSSC were 227 and 473 mAh/g, respectively, when the current density reverted to 0.5 A/g. Noticeably, the NSSC electrode was also stable at a high current density of 1 A/g (Fig. 2g). The electrode delivered 570 mAh/g at 1 A/g and increased to 752 mAh/g after 1050 cycles following three activation cycles at 0.2 A/g.

Electrochemical impedance spectroscopy (EIS) was also performed to investigate the effects of abundant heterointerfaces on the kinetics of NSSC compared to the bare NSS. Fig. 3a and b show the Nyquist plots in different cycles from the 1st to the 30th cycle in the charged state. The curves were fitted using a simple electrical circuit (inset of Fig. 3c), and three important resistances were derived and compared in Fig. 3c and d. These resistances were the initial bulk resistance (R_e), SEI-film resistance (R_{SEI}), and charge-transfer resistance (R_{ct}) [53,57,58].

The R_e value in the 1st cycle of NSS was 50.4 Ω, which decreased to 5.7 Ω in the 2nd cycle and remained unchanged during 30 cycles. However, for the 1st cycle of NSSC, it was as low as 3.5 Ω and diminished to 2.4 Ω, showing no noticeable alteration during the 30 cycles. R_{SEI} for NSS was estimated as 19.6 Ω, 21.8 Ω, 24.7 Ω, 29.6 Ω, 34.7 Ω, 44.4 Ω, and 49.3 Ω in the 1st, 2nd, 5th, 10th, 15th, 20th, and 30th cycles, respectively. In contrast, for NSSC, it was as low as 2.5 Ω in the 1st cycle and slightly increased to 5.7 Ω after 30 cycles, indicating a noticeable 8.5 times decline compared to the bare NSS electrode after the same number of cycles. R_{ct} values for NSS were extremely high, ranging from 89.9 Ω to 232.8 Ω in the 1st to 30th cycles. In contrast, for NSSC, they were 17.5 Ω, 16.5 Ω, 14.4 Ω, 15.1 Ω, 13.7 Ω, 12.1 Ω, and 11.5 Ω for the same number of cycles, respectively.

We further investigated the phase evolution of NSS and NSSC electrodes during lithiation and delithiation reactions. Fig. 4a and b illustrate the XRD patterns of disassembled cells after 1 (both discharging and charging states) and 25 (charging state) cycles. In the discharged NSSC electrode (Fig. 4a), distinct peaks associated with $Li_{22}Sn_5$ and Li_2S phases were identified. The Ni peaks were superimposed with those of the Cu current collector. Notably, prominent diffraction peaks related to Li_2O were also detected after the initial discharging, suggesting the

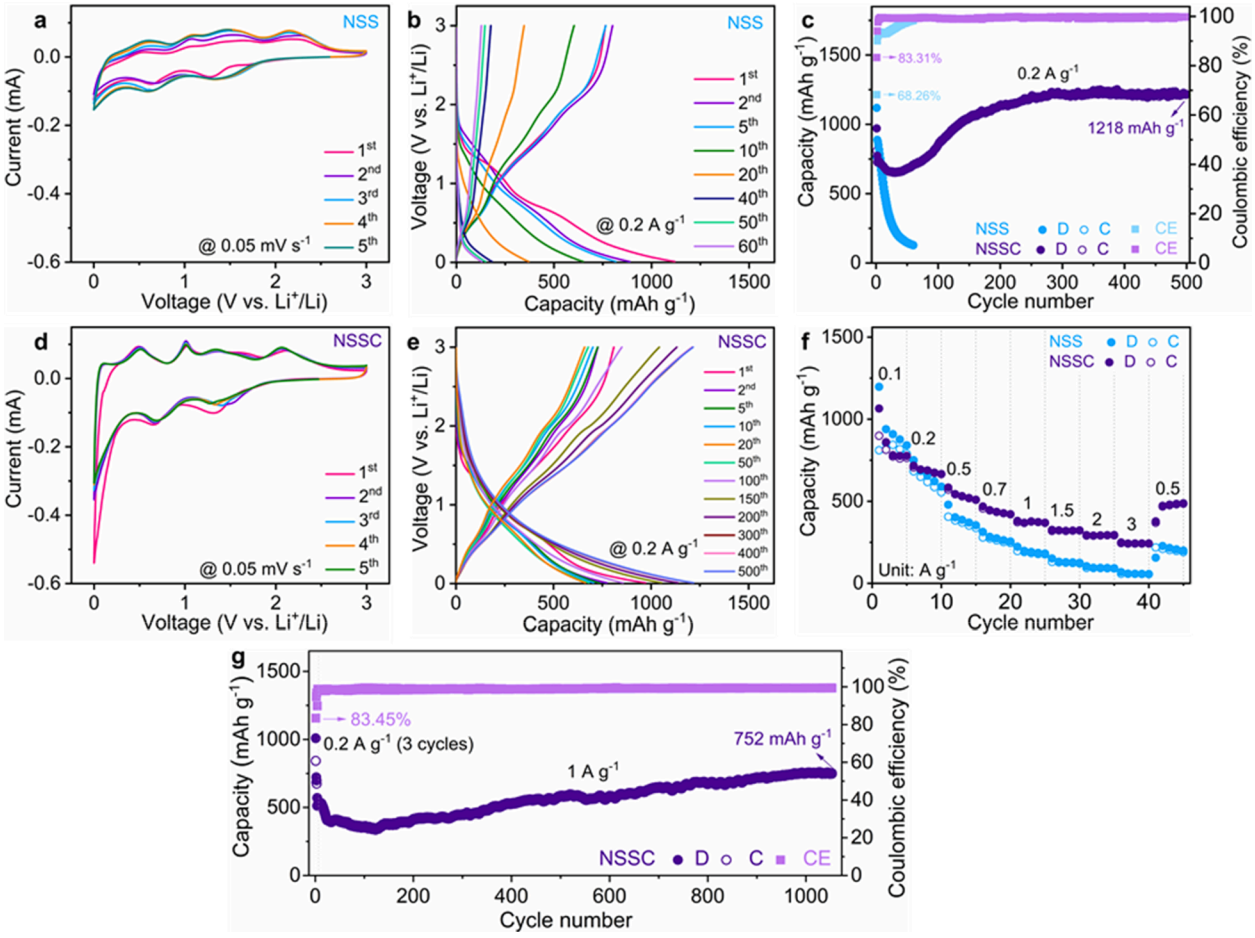

Fig. 2. (a, d) CV curves at 0.05 mV/s, (b, e) charge/discharge curves at 0.2 A/g, (c) cycling performance and the CE values at 0.2 A/g, (f) rate capability at various current densities for NSS and NSSC electrodes, and (g) high-rate cycling stability of NSSC at 1 A/g.

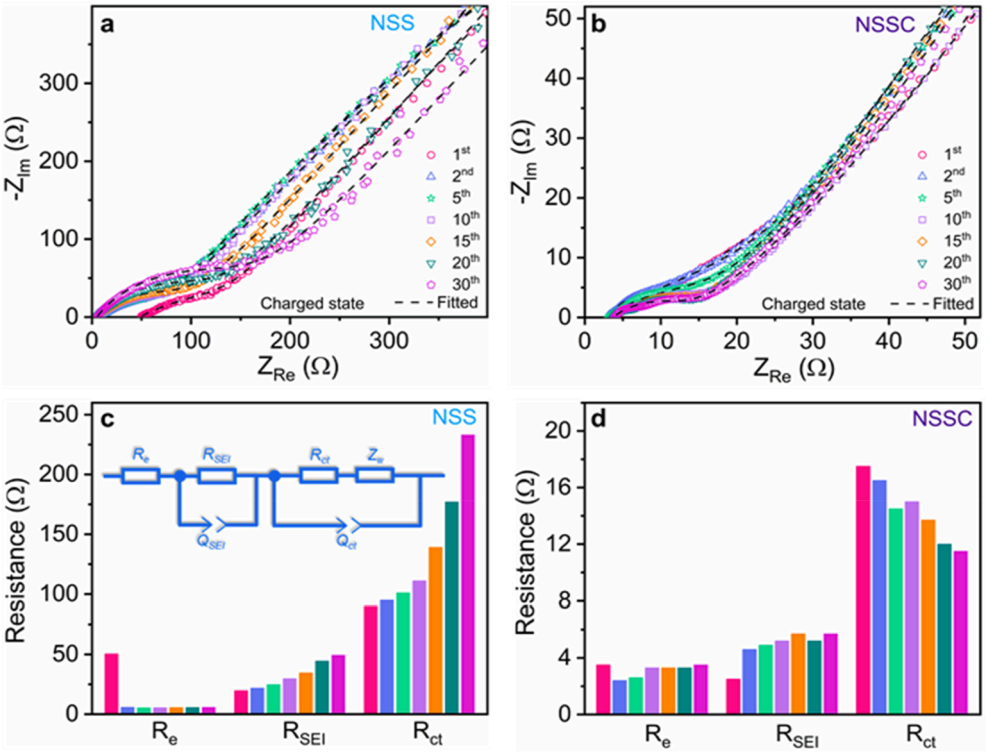

Fig. 3. (a, b) Nyquist plots of NSS and NSSC at different cycles (fully charged state), and (c, d) R_e, R_{SEI}, and R_{ct} values acquired from the plots using a corresponding circuit in the inset of (c).

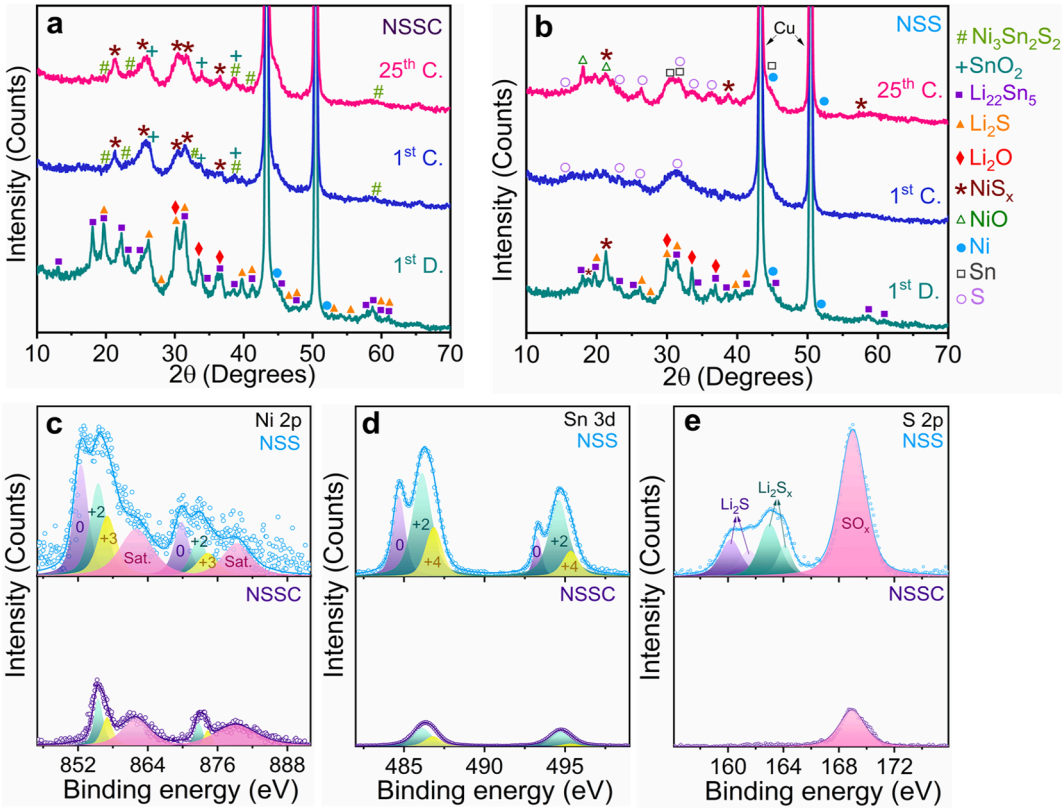

Fig. 4. XRD patterns of disassembled (a) NSSC and (b) NSS electrodes after the 1st discharging, 1st charging, and 25th charging states. High-resolution (c) Ni 2p, (d) Sn 3d, and (e) S 2p XPS spectra for charged NSS and NSSC electrodes after 25 cycles.

reaction of surface oxides with Li^+ to form Li_2O. During recharging, small peaks attributed to $Ni_3Sn_2S_2$ nanoparticles appeared. Furthermore, additional peaks associated with NiS_x (closely matched with Ni_9S_8 and Ni_7S_6) and SnO_2 phases were identified. This indicates that during the recharging process, some Sn nanocrystals reacted with Li_2O to form SnO_2. Additionally, a combination of Ni and S species resulted in the formation of binary nickel sulfides. These recharging products were also observed in the NSSC electrode after 25 cycles. Therefore, the following lithiation/delithiation reactions could be considered for NSSC during cycling tests:

$$Ni + Li_2S + Li_{22}Sn_5 \overset{\leftarrow \text{Discharge/Charge} \rightarrow}{\leftrightarrow} Ni_3Sn_2S_2 \quad (1)$$

$$Sn + Li_2O \overset{\leftarrow \text{Discharge/Charge} \rightarrow}{\leftrightarrow} SnO_2 \quad (2)$$

$$Ni + S \overset{\leftarrow \text{Discharge/Charge} \rightarrow}{\leftrightarrow} NiS_x \quad (3)$$

$$\text{Total (from 2nd cycle)}: Ni + Li_2S + Li_{22}Sn_5 + Li_2O \overset{\leftarrow \text{Discharge/Charge} \rightarrow}{\leftrightarrow} Ni_3Sn_2S_2 + SnO_2 + NiS_x \quad (4)$$

In contrast, Fig. 4b reveals significantly lower intensities of diffraction peaks for $Li_{22}Sn_5$, Li_2S, and Li_2O discharge products in the bare NSS compared to the NSSC hybrid. Moreover, a new large peak at $2\theta = 21.34^\circ$ is observed, which corresponds to NiS_x aggregates. During the first delithiation, $Ni_3Sn_2S_2$ peaks are not present, and only weak peaks of elemental S are identified. This suggests an incomplete oxidation process and irreversible recharging reactions in the bare NSS electrode. After 25 cycles, the recharging products include elemental S, Sn, and Ni, along with new peaks attributed to NiO and NiS_x phases, predominantly Ni_9S_8 and Ni_7S_6. These XRD patterns confirm that the poor reaction kinetics of the bare NSS electrode during both the lithiation and delithiation processes lead to detrimental aggregation of electrode materials. This aggregation causes additional undesirable stress and results in rapid capacity fading during cycling tests.

Fig. 4c-4e present high-resolution XPS spectra for Ni 2p, Sn 3d, and S 2p in charged NSS and NSSC electrodes after 25 cycles, respectively. As observed, the intensities of all the peaks in NSS are significantly higher compared to NSSC, indicating uncontrolled aggregation of nanocrystals in the bare NSS, while the integrity and size of nanoparticles in the NSSC hybrid are maintained after 25 cycles [4,7,57,59,60]. The high-resolution Ni 2p spectra of the NSS electrode show the presence of Ni^0, Ni^{2+}, and Ni^{3+} species, along with satellite peaks. The contribution of Ni^0 is predominant (Fig. 4c), confirming that a large portion of Ni in NSS is in the elemental state, consistent with the XRD patterns. However, the Ni^0 state is negligible in the NSSC hybrid, with only Ni^{2+} and Ni^{3+} valence states present, indicating the formation of $Ni_3Sn_2S_2$ and NiS_x compounds. The Sn 3d spectra of NSS also reveal a prominent Sn^0 peak in addition to Sn^{2+} and Sn^{4+} species, while the Sn 3d spectra of NSSC consist only of Sn^{2+} and Sn^{4+} (Fig. 4d).

Furthermore, high-resolution S 2p spectra for NSS showed a broad peak in the range of 158–166 eV, which could be attributed to the Li_2S and Li_2S_x phases [61]. Moreover, there was another large peak centered at 169 eV due to surface SO_x species. Importantly, the S 2p spectra for NSSC exhibited only a small single peak at 169 eV, without any signals at lower binding energies (Fig. 4e). This may suggest that various lithium polysulfides shifted from the bulk to the surface of the NSS electrode during the cycling test, while the unfavorable shuttle effect was successfully inhibited in the NSSC hybrid. It can also be deduced that the NSSC electrode possessed a strong, stable SEI film, while the bare NSS electrode had a broken, uneven SEI layer, and thus, the surface XPS could collect data from its inner parts [4,31,62].

The charged NSS and NSSC electrodes after 1 and 25 cycles were further probed using the TEM technique to explore the distribution of various components and the probable aggregation in the products. TEM observations revealed that the NSS recharging products were extensively aggregated, and the sizes of individual particles were approximately 10–12 nm after one cycle (Fig. 5a). The recharging products in NSS were severely agglomerated after 25 cycles, generating large clusters (Fig. 5c). Moreover, a thin SEI film covered the NSS electrode materials after one cycle; however, its thickness and compactness were not consistent after 25 cycles (Fig. 5b). In contrast, the recharging products in NSSC were well-dispersed throughout the carbon matrix, and the tiny nanoparticles had average sizes of less than 5 nm after one cycle (Fig. 5d). Twenty-four additional cycles did not show indicators of the collapse of electrode materials, and the generated SEI film remained thin and uniform (Fig. 5e), demonstrating adequate protection of electrode materials during cycling tests. The high-resolution TEM image of NSSC once again verified the fully crystalline nature of the recharging products, as vivid lattice fringes completely matched with $Ni_3Sn_2S_2$ (2 0 2) and (1 1 3), Ni_9S_8 (1 3 1), Ni_7S_6 (1 2 1), and SnO_2 (2 0 0) crystallographic planes (Fig. 5f), in agreement with the XRD pattern. The homogeneous distribution of several nano-sized discharging/recharging products with atomic-level heterointerfaces suitably exhibited buffering and catalytic effects to simultaneously alleviate volumetric changes and promote the redox reactions during repeated cycles [31,63,64].

Fig. 5g and h depict the HAADF-STEM images, their representative overlays, and elemental maps for Ni, Sn, S, O, F, and P of charged NSS and NSSC electrodes after 25 cycles. The HAADF-STEM image of NSS reveals significant aggregation of recharging products. This issue is further elucidated by the Ni-K and Sn-L edges, as the distributions of Ni and Sn differ from that of S, suggesting that NSS mostly experiences irrepressible collapse and agglomeration of these two elements. However, the energy-dispersive spectroscopy (EDS) maps of Ni, Sn, and S for NSSC exhibit a monotonic distribution. Another noticeable difference is the strong signal of the O-K edge in NSS compared to NSSC. Since the recharging products of NSS are not predominantly oxides (except for some small peaks associated with NiO in the XRD pattern), the intense O signal could be attributed to the formation of abundant organic compounds in the SEI layer or the surface oxidation of shuttled/recharged S (Fig. 4e). Additionally, the concentration of F in NSS is higher than that in NSSC, suggesting a greater formation of the inorganic LiF phase in the SEI layer of NSS compared to NSSC. This finding is further supported by the P-K signals in both electrodes, as the P concentration in NSS is higher than in NSSC. This conclusion confirms the essential functions of the carbon network and robust chemical bonds, which stably protect the electrode materials from severe volume variations during cycling and prevent the formation of new surfaces resulting from crack growth and propagation. Thus, the SEI film does not regenerate in the NSSC hybrid during cycling. However, the bare NSS electrode undergoes significant volume expansion, causing the formed SEI films to break and new uncovered electrode surfaces to form. Consequently, continuous electrolyte decomposition leads to the formation of high organic and inorganic phases in the SEI layer (Fig. 5g) with high porosity and non-uniform thickness and morphology (Fig. 5b) [65].

Fig. 6a and d present the anodic state differential capacity (dQ/dV) vs voltage curves of NSS and NSSC electrodes at different cycles (derived

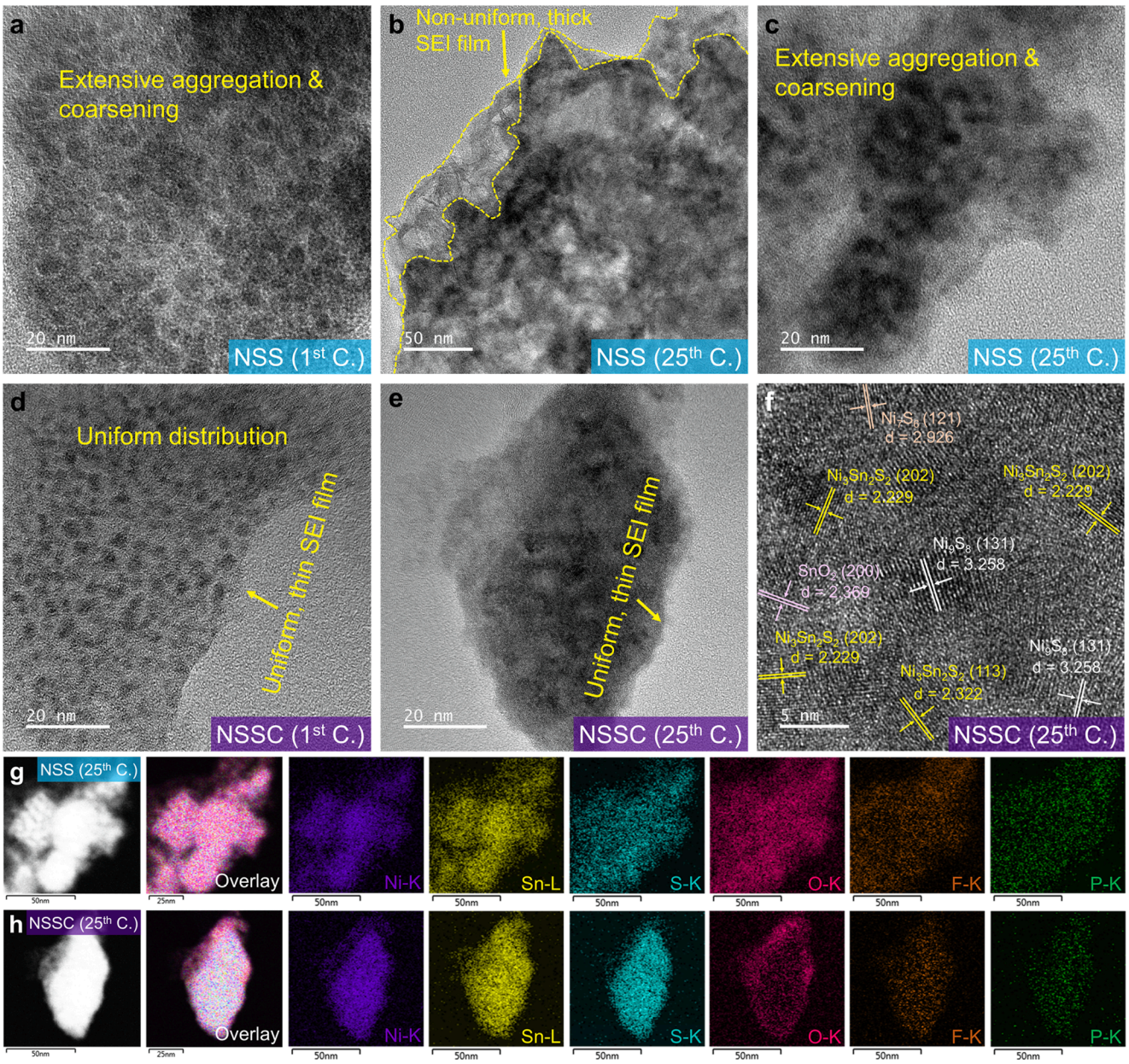

Fig. 5. TEM images of charged (a) NSS and (d) NSSC electrodes after 1 cycle, and charged (b, c) NSS and (e, f) NSSC electrodes after 25 cycles; HAADF-STEM images and their representative overlay images, as well as elemental mapping analysis of Ni, Sn, S, O, F, and P elements for charged (g) NSS and (h) NSSC electrodes after 25 cycles.

from Fig. 2c) to unveil the nature of various redox reactions during the delithiation process. The plots have been divided into four distinct regions: (i) 0.0–0.83, (ii) 0.83–1.76, (iii) 1.76–2.45, and (iv) 2.45–3.0 V, shaded with four different colors in Fig. 6a and d. Based on previous XRD, XPS, and TEM analyses, these four areas can be described as follows: (i) the dealloying reaction of Li_xSn to Sn with a clear peak at around 0.5 V [7,66]; (ii) the conversion reaction of as-formed Sn and Li_2O to generate SnO_2 nanocrystals [6,7,66]; (iii) the multi-step conversion reactions of Li_xS phases to produce elemental S [61], concurrent with the reconstruction of $Ni_3Sn_2S_2$ (in NSSC hybrid only), various nickel sulfides (mostly Ni_9S_8 and Ni_7S_6) [67], and oxidation of Ni (as observed for NSS only) [23]; and (iv) pseudocapacitive Li storage and electrolyte decomposition at potentials higher than 2.5 V [57,67]. These anodic reactions align with those mentioned above (Equations (1) to (4)) for the NSSC hybrid (Fig. 6d). However, the delithiation reactions were found to be irreversible for the bare NSS during cycling (Fig. 6a) and provide a thorough explanation for the rapid capacity decay shown in Fig. 2c.

The charge capacities of the two electrodes were calculated for voltage ranges of 0.0–0.83, 0.83–1.76, 1.76–2.45, and 2.45–3.0 V, as depicted in Fig. 6b, 6c, 6e, and 6f. In the first area (i) (Fig. 6b), the initial charge capacity for NSS was 167 mAh/g, which remained relatively stable for 10 cycles at 164 mAh/g. However, after 20 and 50 cycles, the capacity decreased to 129 and 73 mAh/g, respectively. For NSSC in the same section, the first charge capacity was 189 mAh/g. It decreased to 157 and 150 mAh/g after 10 and 20 cycles, respectively. However, after 50, 100, 200, 400, and 500 cycles, the capacity increased to 174, 205, 246, 253, and 254 mAh/g, respectively. In section (ii), the capacity of NSS continuously decreased during cycling from 322 mAh/g in the 1st cycle to 233, 110, and 36 mAh/g after 10, 20, and 50 cycles, respectively. For NSSC, the charge capacities decreased from 323 mAh/g in the 1st cycle to 263, 245, and 235 mAh/g after 10, 20, and 50 cycles,

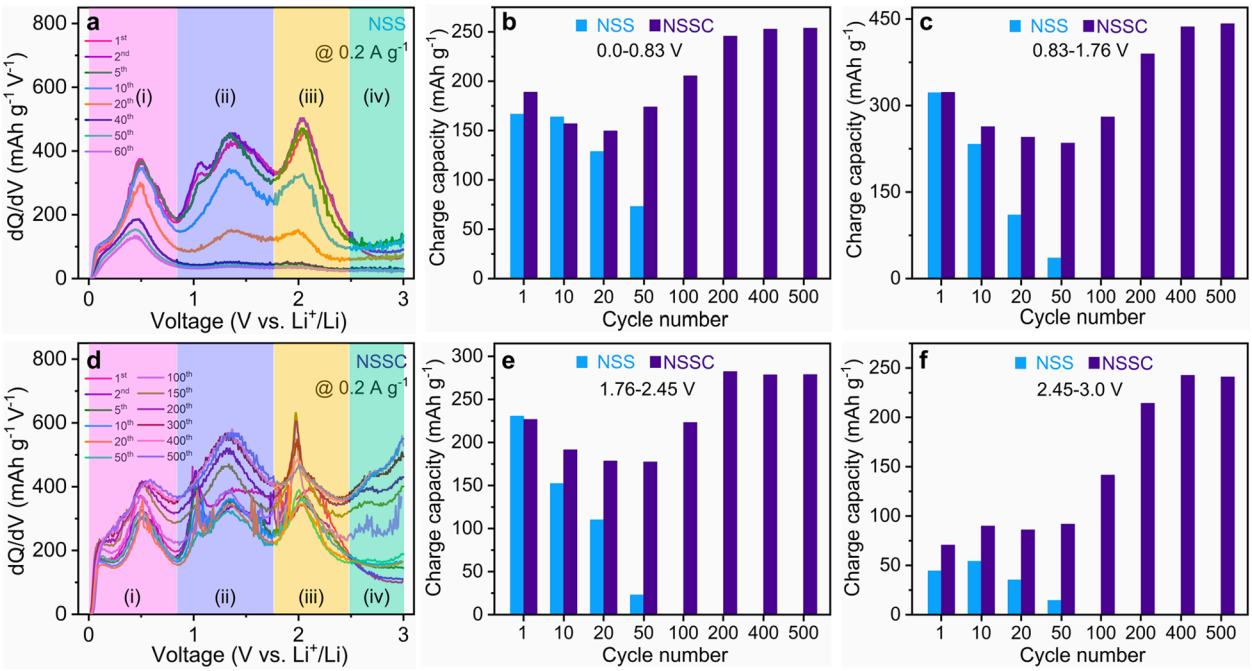

Fig. 6. (a, d) dQ/dV vs voltage curves (charge state) of NSS and NSSC electrodes at different cycles (derived from Fig. 2c). Charge capacities of the two electrodes for voltage ranges of (b) 0.0–0.83, (c) 0.83–1.76, (e) 1.76–2.45, and (f) 2.45–3.0 V.

respectively. However, after 100, 200, 400, and 500 cycles, the capacities increased to 280, 390, 437, and 442 mAh/g (Fig. 6c). In region (iii), as shown in Fig. 6e, NSS delivered 231, 152, 110, and 23 mAh/g after 1, 10, 20, and 50 cycles, respectively. On the other hand, NSSC exhibited 227, 191, 179, 177, 223, 282, 279, and 279 mAh/g after 1, 10, 20, 50, 100, 200, 400, and 500 cycles, respectively. In the last area (iv) (Fig. 6f), NSS showed insignificant capacity values lower than 55 mAh/g. In contrast, NSSC delivered 71, 90, 86, 92, 142, 214, 246, and 241 mAh/g after 1, 10, 20, 50, 100, 200, 400, and 500 cycles, respectively. The unexpected formation of Li_2O during discharging and SnO_2 and NiS_x phases during recharging caused additional redox reactions in NSSC, which align with reactions (1) to (4) and explain the unusual cycling performance observed in Fig. 2c.

Negative-mode depth time-of-flight secondary ion mass spectrometry (ToF-SIMS) was conducted to demonstrate the chemical bonds between $Ni_3Sn_2S_2$ nanoparticles and the CNT network in the cycled NSSC electrode. Fig. 7a provided evidence of persistent $SnOC^-$, SOC^-, and $NiOC^-$ chemical bonds at the atomic level between the two components, $Ni_3Sn_2S_2$ and CNT, in NSSC after 25 cycles. This guarantees the continuous occurrence of pseudocapacitive Li storage at numerous heterointerfaces, thereby promoting the kinetics of the redox reactions and mitigating the large volume changes during cycling tests. Particularly at high current rates, as observed in Fig. 2g, the pseudocapacitive Li storage exhibited a predominant contribution, enabling rapid and reversible Li^+ insertion/extraction processes for over 1000 cycles [45,68–70]. In Fig. 7b, strong signals of polysulfide intermediates were depicted for the bare NSS electrode, with $Li_2S_5^-$ showing the highest intensity. A significant Li_2S^- signal was also identified in the depth profile, indicating the incomplete recharging reaction that converts discharge products to elemental S [4,62]. In contrast, no indications of polysulfide phases were detected for the NSSC electrode, confirming the complete conversion of lithium polysulfides to recharging products and their limited movement from the bulk to the electrode surface [61].

Depth ToF-SIMS was also utilized to examine the organic and inorganic compounds in the SEI films of NSS and NSSC electrodes after 25 cycles (Fig. 7c,d). The bare NSS electrode exhibited strong fragments of SO^-, LiF^-, and $Li_2CO_3^-$, while the contributions of Li_2F^- and Li_2O^- signals were negligible. The SO^- signal likely originated from the oxidation of recharged S particles or intermediate polysulfides, as these particles were not protected by the carbon network and inevitably came into excessive contact with the electrolyte during cycling. The high fragments of LiF^- and $Li_2CO_3^-$ indicated that the bare NSS electrode could not maintain its integrity during cycling, leading to continuous electrolyte decomposition and SEI formation on newly generated surfaces (Fig. 7e) [57,71].

In addition, high signals of $C_3H_2^-$, C_3H^-, CHO_2^-, C_2HO^-, and CHO^- fragments were observed in the charged NSS electrode after 25 cycles, verifying the high content of organic compounds in its SEI film. Notably, the CHO_2^- and C_2HO^- signals exhibited very high intensities (Fig. 7d, top panel). These findings align perfectly with the HAADF-STEM image of the cycled NSS electrode and its EDS mapping analysis (Fig. 5g). In contrast, NSSC displayed uniform LiF^- and Li_2O^- signals, with insignificant presence of SO^- and $Li_2CO_3^-$ phases (Fig. 7c, bottom panel). Organic compounds were also evenly distributed in the SEI film of the NSSC electrode (Fig. 7d, bottom panel). Thus, it can be inferred that the NSSC hybrid consisted of both organic and inorganic phases. The inorganic compounds formed a robust and stable SEI layer, safeguarding the electrode materials against significant volume changes during cycling. Furthermore, the uniform distribution of organic species facilitated ion transport and reduced side reactions on the surface of the electrode materials [72,73]. Consequently, it can be concluded that the NSSC hybrid, with its strong chemical bridges, exhibited metallic-type conductivity, excellent structural integrity, improved pathways for ion and electron transport, and abundant electrochemically reactive sites with additional anodic/cathodic redox reactions. As a result, the NSSC heterostructure effectively prevented the aggregation of Ni and Sn nanoparticles and mitigated the unfavorable oxidation and shuttling of polysulfides, thereby achieving highly reversible Li storage performance.

3. Conclusions

This study successfully fabricated an innovative Janus-type NSSC heterostructure with permanent Ni-O-C, Sn-O-C, and S-O-C chemical connections through a quick, versatile microwave irradiation technique and subsequent ball milling. In this binary Janus-type heterostructure,

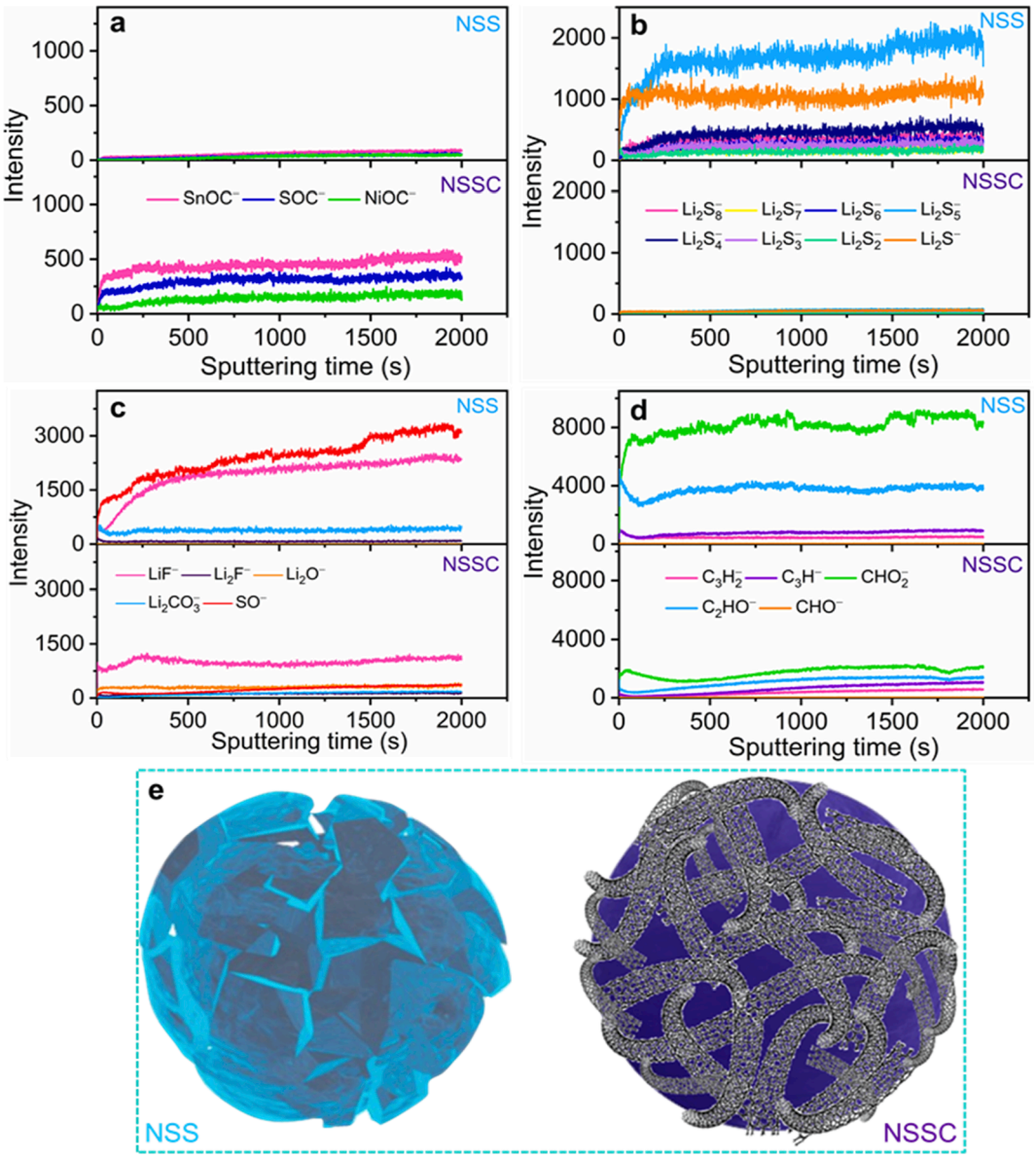

Fig. 7. Depth profiles of ToF-SIMS analysis for (a) $SnOC^-$, SOC^-, and $NiOC^-$; (b) $Li_2S_8^-$, $Li_2S_7^-$, $Li_2S_6^-$, $Li_2S_5^-$, $Li_2S_4^-$, $Li_2S_3^-$, $Li_2S_2^-$, and Li_2S^-; (c) LiF^-, Li_2F^-, Li_2O^-, $Li_2CO_3^-$, and SO^-; (d) $C_3H_2^-$, C_3H^-, CHO_2^-, C_2HO^-, and CHO^- fragments of charged NSS and NSSC electrodes after 25 cycles; and (e) schematic structural differences between bare NSS and Janus-type NSSC heterostructure after long-term cycles.

both the $Ni_3Sn_2S_2$ and CNTs possessed excellent conductivity due to their metallic nature. Additionally, CNTs preserved the integrity of electrode materials, prevented the aggregation of Ni and Sn nanocrystals, suppressed the oxidation and movement of intermediate polysulfides, enhanced Li^+ transport pathways, and improved surface pseudocapacitive Li^+ storage through plentiful extra active sites. Moreover, $Ni_3Sn_2S_2$ acted as a high-capacity material and provided reversible Li^+ storage performance for durable cycles. When the NSSC heterostructure was employed as an anode in half-cell LIBs, a thin, monotonic organic/inorganic-rich SEI film was generated on the outermost surface of active materials. Furthermore, it fully protected the discharging/recharging products, thus delivering high ICE (>83 %) and ultrastable long-term cycling stability (1218 mAh/g after 500 cycles at 0.2 A/g and 752 mAh/g after 1050 cycles at 1 A/g). This study offers a deeper understanding of the efficient exploitation of multi-component alloying and conversion-type electrode materials for high-performance metal-ion batteries.

4. Experimental section

4.1. Synthesis

The synthesis of the NSS nanoparticles was carried out using a microwave method. $NiCl_2{\cdot}6H_2O$ (Merck, ≥98.0 %), $SnCl_2{\cdot}2H_2O$ (Merck, ≥99.0 %), and CH_4N_2S (Merck, ≥99.0 %) were employed as precursors for Ni, Sn, and S, respectively. The solvent used was DEG (Merck, ≥98.0 %). Initially, 3.56 g of $NiCl_2{\cdot}6H_2O$, 2.26 g of $SnCl_2{\cdot}2H_2O$, and 0.76 g of CH_4N_2S were added separately to 100 mL of DEG at a temperature of 50 °C, with each precursor being allowed to completely dissolve before the next addition. The resulting mixture was stirred for 30 min at this temperature to achieve a homogeneous solution. Subsequently, 1.89 g of $NaBH_4$ (Merck, ≥98.0 %) was added as a reducing agent and stirred for several minutes. The solution was then transferred to a microwave oven operating at 1200 W and 2.45 GHz, and microwave irradiation was applied under nominal atmospheric conditions for 8 min. Afterward, the solution was allowed to cool naturally to room temperature while inside

the oven. Finally, it was centrifuged and washed several times with distilled water and ethanol. The as-synthesized black powder was dried overnight in an air oven.

In the next step, the NSS powder was mixed with commercial multi-walled CNTs in a weight ratio of 7:3. The mixture was then subjected to ball milling (using a Fritsch *P*6 planetary ball mill) for 10 h at a speed of 300 rpm, with a ball-to-powder weight ratio of 20:1.

4.2. Structural characterization

XRD patterns were obtained from a Rigaku diffractometer using Cu K_α radiation. XPS measurements were performed on a K-alpha spectrometer (Thermo Scientific Inc.) using monochromated Al K_α radiation. TEM analysis, along with EDS and SAED analyses, was conducted using a Cs-corrected-STEM (JEM-ARM 200F, JEOL) operating at a voltage of 200 kV. Depth ToF-SIMS measurements (ToF-SIMS 5 spectrometer, ION-TOF) were obtained by applying a Bi_3^{2+} beam in negative mode within a m/z range of 0–500, with an examined area of 100 μm × 100 μm.

4.3. Electrochemical characterization

Electrochemical tests were performed using coin-type CR2032 half-cells with Li metal as the counter electrode. The electrode slurry consisted of a homogeneous mixture of electrode materials (NSS or NSSC), carbon black, and binder in a weight ratio of 75:15:15. A binder comprising a mixture of sodium carboxyl methyl cellulose (1 wt% in H_2O) and poly(acrylic acid) (3 wt% in H_2O) in a weight ratio of 1:1 was used. The prepared slurry was pasted onto a Cu foil using a doctor blade and dried for 3 h at 150 °C in a vacuum oven. The electrolyte consisted of a 1 M lithium hexafluorophosphate dissolved in a ternary solvent mixture of ethylene carbonate, dimethyl carbonate, and diethyl carbonate in a volume ratio of 2:2:1, with an additional 10 % fluoroethylene carbonate. Polypropylene (Celgard 2400) was employed as the separator. A potentiostat/galvanostat with a cut-off voltage of 0.01–3 V (vs Li^+/Li) was used for CV, charge/discharge, and EIS analyses. The cycled cells were disassembled in an Ar-filled glovebox for post-LIB characterizations. The electrodes were rinsed with dimethyl carbonate and dried at room temperature inside the glovebox.

4.4. Calculations

The projector-augmented wave method implemented in the Quantum-ESPRESSO package from Materials Square was utilized for conducting density functional theory calculations. The Perdew-Burke-Ernzerhof exchange–correlation functionals were adopted. The spin-polarized $Ni_3Sn_2S_2$ supercell consisted of Ni, Sn, and S with valence electron configurations of $3d^84s^2$, $4d^{10}5s^25p^2$, and $3s^23p^4$, respectively. The cut-off energy was set to 300 Ry, and the electron wavefunction was set to 50 Ry. To accelerate the computation of electronic energy near the Fermi level, Gaussian smearing with a width of 0.002 Ry was employed during the relaxation of the $Ni_3Sn_2S_2$ structure. Brillouin zone integration was performed using a Monkhorst-Pack method with k-point meshes of 5 × 5 × 2. For the analysis of the density of states, the first Brillouin zone was verified with a grid spacing of 11 × 11 × 5 based on a unique Monkhorst-Pack k-point scheme.

CRediT authorship contribution statement

Niloofar Kolivand: Investigation, Methodology, Formal analysis, Writing – original draft. **Safa Haghighat-Shishavan:** Investigation, Methodology, Software, Formal analysis, Writing – original draft. **Mahboobeh Nazarian-Samani:** Investigation, Formal analysis, Validation, Writing – review & editing. **Mehdi Kheradmandfard:** Investigation, Methodology. **Masoud Nazarian-Samani:** Conceptualization, Methodology, Software, Writing – review & editing, Supervision. **Seyed Farshid Kashani-Bozorg:** Writing – review & editing, Supervision, Funding acquisition. **Wooyoung Lee:** Writing – review & editing, Supervision, Funding acquisition.

Declaration of Competing Interest

The authors declare that they have no known competing financial interests or personal relationships that could have appeared to influence the work reported in this paper.

Data availability

Data will be made available on request.

Acknowledgments

This research was financially supported by the Technology Innovation Program (Program No. 20013621, Center for Super Critical Material Industrial Technology) funded by the Ministry of Trade, Industry & Energy (MOTIE, Korea); Nano·Material Technology Development Program through the National Research Foundation of Korea (NRF) funded by the Ministry of Science and ICT (NRF-2022M3H4A3053304); and Basic Science Research Program through the National Research Foundation of Korea (NRF) funded by the Ministry of Education (NRF-2019R1A6A1A11055660).

Appendix A. Supplementary data

Supplementary data to this article can be found online at https://doi.org/10.1016/j.jcis.2023.05.176.

References

[1] S. Liang, Y.-J. Cheng, J. Zhu, Y. Xia, P. Müller-Buschbaum, A chronicle review of nonsilicon (Sn, Sb, Ge)-based lithium/sodium-ion battery alloying anodes, Small Methods. 4 (2020) 2000218.
[2] X. Gao, X. Liu, R. He, M. Wang, W. Xie, N.P. Brandon, B. Wu, H. Ling, S. Yang, Designed high-performance lithium-ion battery electrodes using a novel hybrid model-data driven approach, Energy Storage Mater. 36 (2021) 435–458.
[3] G.D. Park, J.-S. Park, J.K. Kim, Y.C. Kang, Recent advances in heterostructured anode materials with multiple anions for advanced alkali-ion batteries, Adv. Energy Mater. 11 (2021) 2003058.
[4] S. Haghighat-Shishavan, M. Nazarian-Samani, M. Nazarian-Samani, S.H. Hosseini-Shokouh, T. Maschmeyer, K.-B. Kim, Realization of $Sn_2P_2S_6$-carbon nanotube anode with high K^+/Na^+ storage performance via rational interface manipulation-induced shuttle-effect inhibition and self-healing, Chem. Eng. J. 435 (2022), 134965.
[5] S. Zhao, Y. He, Z. Wang, X. Bo, S. Hao, Y. Yuan, H. Jin, S. Wang, Z. Lin, Advancing performance and unfolding mechanism of lithium and sodium storage in SnO_2 via precision synthesis of monodisperse PEG-ligated nanoparticles, Adv. Energy Mater. 12 (2022) 2201015.
[6] X. Lan, X. Xiong, J. Liu, B. Yuan, R. Hu, M. Zhu, Insight into reversible conversion reactions in SnO_2-based anodes for lithium storage: A review, Small 18 (2022) 2201110.
[7] S. Zhao, C.D. Sewell, R. Liu, S. Jia, Z. Wang, Y. He, K. Yuan, H. Jin, S. Wang, X. Liu, Z. Lin, SnO_2 as advanced anode of alkali-ion batteries: Inhibiting Sn coarsening by crafting robust physical barriers, void boundaries, and heterophase interfaces for superior electrochemical reaction reversibility, Adv. Energy Mater. 10 (2020) 1902657.
[8] X. Wu, X. Lan, R. Hu, Y. Yao, Y. Yu, M. Zhu, Tin-based anode materials for stable sodium storage: Progress and perspective, Adv. Mater. 34 (2022) 2106895.
[9] H. Liang, J. Ni, L. Li, Bio-inspired engineering of Bi_2S_3-PPy yolk-shell composite for highly durable lithium and sodium storage, Nano Energy 33 (2017) 213–220.
[10] J. Li, L. Han, X. Zhang, H. Sun, X. Liu, T. Lu, Y. Yao, L. Pan, Multi-role TiO_2 layer coated carbon@few-layered MoS_2 nanotubes for durable lithium storage, Chem. Eng. J. 406 (2021), 126873.
[11] N. Deng, Y. Li, Q. Li, Q. Zeng, S. Luo, H. Wang, W. Kang, B. Cheng, Multi-functional yolk-shell structured materials and their applications for high-performance lithium ion battery and lithium sulfur battery, Energy Storage Mater. 53 (2022) 684–743.
[12] Y.-Q. Wu, Y.-S. Zhao, W.-J. Meng, Y. Xie, J. Zhang, C.-J. He, D.-L. Zhao, Nanoplates-assembled SnS_2 nanoflowers with carbon coating anchored on reduced graphene oxide for high performance Li-ion batteries, Appl. Surf. Sci. 539 (2021), 148283.
[13] A. Aziz, P. Mangelis, P. Vaqueiro, A.V. Powell, R. Grau-Crespo, Electron and phonon transport in shandite-structured $Ni_3Sn_2S_2$, Phys. Rev. B. 94 (2016), 165131.

[14] Y. Shan, X. Sun, F. Liu, L. Liu, Non-bonding electronic reconfiguration by surface engineering in shandite $A_3M_2S_2$ (A=Fe, Co; M=In, Sn) for hydrogen evolution reaction, Mater. Chem. Phys. 290 (2022), 126565.

[15] M.A. McGuire, Q. Zhang, H. Miao, W. Luo, M. Yoon, Y. Liu, T. Yilmaz, E. Vescovo, Antiferromagnetic order and linear magnetoresistance in Fe-substituted shandite $Co_3In_2S_2$, Chem. Mater. 33 (2021) 9741–9749.

[16] Y. Yanagi, J. Ikeda, K. Fujiwara, K. Nomura, A. Tsukazaki, M.-T. Suzuki, First-principles investigation of magnetic and transport properties in hole-doped shandite compounds $Co_3In_xSn_{2-x}S_2$, Phys. Rev. B 103 (2021), 205112.

[17] P. Mangelis, P. Vaqueiro, A.V. Powell, Improved thermoelectric performance through double substitution in shandite-type mixed-metal sulfides, ACS Appl. Energy Mater. 3 (2020) 2168–2174.

[18] M. Tanaka, Y. Fujishiro, M. Mogi, Y. Kaneko, T. Yokosawa, N. Kanazawa, S. Minami, T. Koretsune, R. Arita, S. Tarucha, M. Yamamoto, Y. Tokura, Topological kagome magnet $Co_3Sn_2S_2$ thin flakes with high electron mobility and large anomalous Hall effect, Nano Lett. 20 (2020) 7476–7481.

[19] S. Chaouch, A. Othmani, R. Rahmani, A. Boukhachem, N. Kamoun Turki, M. Amlouk, Low-cost route synthesis, structural, electrical and electrochemical investigations on shandite $Ni_3Sn_2S_2$ sprayed thin film, Optik (Stuttg) 232 (2021), 166517.

[20] D. Zhou, X. Guo, Q. Zhang, Y. Shi, H. Zhang, C. Yu, H. Pang, Nickel-based materials for advanced rechargeable batteries, Adv. Funct. Mater. 32 (2022) 2107928.

[21] J. He, A. Bhargav, A. Manthiram, High-energy-density, long-life lithium-sulfur batteries with practically necessary parameters enabled by low-cost Fe-Ni nanoalloy catalysts, ACS Nano. 15 (2021) 8583–8591.

[22] A. Esfandiari, S. Haghighat-Shishavan, M. Nazarian-Samani, M. Nazarian-Samani, S. Ramakrishna, S.F. Kashani-Bozorg, K.-B. Kim, Defect-rich Ni_3Sn_4 quantum dots anchored on graphene sheets exhibiting unexpected reversible conversion reactions with exceptional lithium and sodium storage performance, Appl. Surf. Sci. 526 (2020), 146756.

[23] Y. Jiang, Y. Li, P. Zhou, S. Yu, W. Sun, S. Dou, Enhanced reaction kinetics and structure integrity of Ni/SnO_2 nanocluster toward high-performance lithium storage, ACS Appl. Mater. Interfaces 7 (2015) 26367–26373.

[24] L. Ma, R. Hu, C. Kang, L. Fu, Y. Chen, H. Liu, Q. Liu, Facile synthesis of three-dimensional $Ni_3Sn_2S_2$ as a novel battery-type electrode material for high-performance supercapacitors, Electrochim. Acta 396 (2021), 139216.

[25] S.-Y. Lu, S. Li, M. Jin, J. Gao, Y. Zhang, Greatly boosting electrochemical hydrogen evolution reaction over Ni_3S_2 nanosheets rationally decorated by $Ni_3Sn_2S_2$ quantum dots, Appl. Catal. B Environ. 267 (2020), 118675.

[26] S.C. Sekhar, B. Ramulu, S.J. Arbaz, S.H. Jin, H.S. Oh, J.S. Yu, Nanosilver-particles integrated $Ni_3Sn_2S_2$-CoS composite as an advanced electrode for high energy density hybrid cell, Small Methods. 5 (2021) 2100907.

[27] D.-Q. Cai, Y.-T. Gao, X.-Y. Wang, J.-L. Yang, S.-X. Zhao, Built-in electric field on the Mott-Schottky heterointerface-enabled fast kinetics lithium-sulfur batteries, ACS Appl. Mater. Interfaces 14 (2022) 38651–38659.

[28] W. Li, Q. Song, M. Li, Y. Yuan, J. Zhang, N. Wang, Z. Yang, J. Huang, J. Lu, X. Li, Chemical heterointerface engineering on hybrid electrode materials for electrochemical energy storage, Small Methods. 5 (2021) 2100444.

[29] H. Wang, C. Wang, Y. Tang, Interface engineering toward high-efficiency alloy anode for next-generation energy storage device, EcoMat. 3 (2021) e12172.

[30] S. Li, L. Zhang, W. Zhao, S. Yuan, L. Yang, X. Chen, P. Ge, W. Sun, X. Ji, Designing interfacial chemical bonds towards advanced metal-based energy-storage/conversion materials, Energy Storage Mater. 32 (2020) 477–496.

[31] S. Haghighat-Shishavan, M. Nazarian-Samani, M. Nazarian-Samani, K.-B. Kim, Electrolyte modulation of $BiPS_4$ concurrently suppressing the Bi coarsening and polysulfide shuttle effect in K-ion batteries, Energy Storage Mater. 39 (2021) 96–107.

[32] M. Nazarian-Samani, H. Abdollah-Pour, O. Mirzaee, A.R. Kamali, M. Nazarian-Samani, Effects of Ni addition on the microstructure and properties of nanostructured copper-germanium alloys, Intermetallics 38 (2013) 80–87.

[33] L. Yan, X. Yang, Y. Zhang, Y. Wu, Z. Cheng, S.B. Darling, L. Shao, Porous Janus materials with unique asymmetries and functionality, Mater. Today 51 (2021) 626–647.

[34] D. Vikraman, S. Hussain, I. Rabani, A. Feroze, M. Ali, Y.-S. Seo, S.-H. Chun, J. Jung, H.-S. Kim, Engineering $MoTe_2$ and Janus SeMoTe nanosheet structures: First-principles roadmap and practical uses in hydrogen evolution reactions and symmetric supercapacitors, Nano Energy 87 (2021), 106161.

[35] C. Li, Z. Sun, T. Yang, L. Yu, N. Wei, Z. Tian, J. Cai, J. Lv, Y. Shao, M.H. Rümmeli, J. Sun, Z. Liu, Directly grown vertical graphene carpets as Janus separators toward stabilized Zn metal anodes, Adv. Mater. 32 (2020) 2003425.

[36] S. Hou, X. Xu, M. Wang, Y. Xu, T. Lu, Y. Yao, L. Pan, Carbon-incorporated Janus-type Ni_2P/Ni hollow spheres for high performance hybrid supercapacitors, J. Mater. Chem. A 5 (2017) 19054–19061.

[37] J. Cao, J. Li, D. Li, Z. Yuan, Y. Zhang, V. Shulga, Z. Sun, W. Han, Strongly coupled 2D transition metal chalcogenide-MXene-carbonaceous nanoribbon heterostructures with ultrafast ion transport for boosting sodium/potassium ions storage, Nano-Micro Lett. 13 (2021) 113.

[38] Y. Ko, H.-I. Kim, S.-J. Cho, K.M. Lee, G.Y. Jung, H. Park, S.H. Park, Y.J. Lee, Y. Bae, Y.-R. Lee, K. Kim, S.K. Kwak, S.-Y. Lee, K. Kang, Liquid-based Janus electrolyte for sustainable redox mediation in lithium-oxygen batteries, Adv. Energy Mater. 11 (2021) 2102096.

[39] M. Nazarian-Samani, H.-D. Lim, S. Haghighat-Shishavan, H.-K. Kim, Y. Ko, M.-S. Kim, S.-W. Lee, S.F. Kashani-Bozorg, M. Abbasi, H.-U. Guim, D.-I. Kim, K.-C. Roh, K. Kang, K.-B. Kim, A robust design of Ru quantum dot/N-doped holey graphene for efficient Li-O_2 batteries, J. Mater. Chem. A 5 (2017) 619–631.

[40] D. Wu, B. Yang, H. Chen, E. Ruckenstein, Nitrogenated holey graphene C_2N monolayer anodes for lithium- and sodium-ion batteries with high performance, Energy Storage Mater. 16 (2019) 574–580.

[41] M. Ben Yahia, J. Vergnet, M. Saubanère, M.-L. Doublet, Unified picture of anionic redox in Li/Na-ion batteries, Nat. Mater. 18 (2019) 496–502.

[42] S. Sarker, D.K. Macharia, Y. Zhang, Y. Zhu, X. Li, M. Wen, R. Meng, N. Yu, Z. Chen, M. Zhu, Synthesis of MnO_2-Ag nanojunctions with plasmon-enhanced photocatalytic and photothermal effects for constructing rewritable mono-/multi-color fabrics, ACS Appl. Mater. Interfaces 14 (2022) 5545–5557.

[43] K. Zhang, J.M. Suh, J.-W. Choi, H.W. Jang, M. Shokouhimehr, R.S. Varma, Recent advances in the nanocatalyst-assisted $NaBH_4$ reduction of nitroaromatics in water, ACS Omega 4 (2019) 483–495.

[44] J. Zhang, Y. Wang, J. Cui, J. Wu, Y. Li, T. Zhu, H. Kang, J. Yang, J. Sun, Y. Qin, Y. Zhang, P.M. Ajayan, Y. Wu, Water-soluble defect-rich MoS_2 ultrathin nanosheets for enhanced hydrogen evolution, J. Phys. Chem. Lett. 10 (2019) 3282–3289.

[45] M. Nazarian-Samani, S. Haghighat-Shishavan, M. Nazarian-Samani, S.F. Kashani-Bozorg, S. Ramakrishna, K.-B. Kim, Perforated two-dimensional nanoarchitectures for next-generation batteries: Recent advances and extensible perspectives, Prog. Mater Sci. 116 (2021), 100716.

[46] Y. Li, F.-M. Li, X.-Y. Meng, X.-R. Wu, S.-N. Li, Y. Chen, Direct chemical synthesis of ultrathin holey iron doped cobalt oxide nanosheets on nickel foam for oxygen evolution reaction, Nano Energy 54 (2018) 238–250.

[47] M. Nazarian-Samani, R. Mobarra, A.R. Kamali, M. Nazarian-Samani, Structural evolution of nanocrystalline nickel-tungsten alloys upon mechanical alloying with subsequent annealing, Metall. Mater. Trans. A 45 (2014) 510–521.

[48] M.-S. Balogun, H. Yang, Y. Luo, W. Qiu, Y. Huang, Z.-Q. Liu, Y. Tong, Achieving high gravimetric energy density for flexible lithium-ion batteries facilitated by core-double-shell electrodes, Energ. Environ. Sci. 11 (2018) 1859–1869.

[49] X. Ou, Z. Xiao, J.-F. Zhang, C. Wang, D. Wang, B. Zhang, Y. Wu, Enhancing the rapid Na^+-storage performance via electron/ion bridges through GeS_2/graphene heterojunction, ACS Nano 14 (2020) 13952–13963.

[50] S. Yin, Y. Wang, X. Zhang, C. Wei, X. Huang, G. Wen, External and internal cultivation: Design for Mo-doped SnS_2/SnO_2 heterostructure on N-doped graphene achieves kinetics-enhanced and superior-lithium storage performance, Appl. Surf. Sci. 609 (2023), 155435.

[51] X. Xu, Y. Zhou, H. You, H. Min, X. Wu, W. Zang, J. Hao, Z. Feng, X. Liu, H. Yang, Engineering nano-NiS_2 embedded in graphitized carbon skeleton in hollow spherical structure as stable anode material for reversible Li^+ storage, Appl. Surf. Sci. 605 (2022), 154758.

[52] C. Wang, Q. Han, R. Xie, B. Wang, T. He, W. Xie, Q. Tang, Y. Li, J. Xu, B. Yu, Fabrication of petal-like Ni_3S_2 nanosheets on 3D carbon nanotube foams as high-performance anode materials for Li-ion batteries, Electrochim. Acta 331 (2020), 135383.

[53] M. Nazarian-Samani, M. Nazarian-Samani, S. Haghighat-Shishavan, K.-B. Kim, Efficient stress alleviation and interface regulation in Cu_4SiP_8-CNT hybrid for ultra-durable Li and Na storage, Nano Energy 86 (2021), 106134.

[54] A. Eftekhari, Low voltage anode materials for lithium-ion batteries, Energy Storage Mater. 7 (2017) 157–180.

[55] W. Zhang, R. Du, C. Zhou, S. Pu, B. Han, K. Xia, Q. Gao, J. Wu, Ultrafine SnO_2 aggregates in interior of porous carbon nanotubes as high-performance anode materials of lithium-ion batteries, Mater. Today Energy. 12 (2019) 303–310.

[56] Y. Liu, Z. Chen, H. Jia, H. Xu, M. Liu, R. Wu, Iron-doping-induced phase transformation in dual-carbon-confined cobalt diselenide enabling superior lithium storage, ACS Nano 13 (2019) 6113–6124.

[57] M. Nazarian-Samani, M. Nazarian-Samani, S. Haghighat-Shishavan, K.-B. Kim, Si, P vacancy-enriched $CoSi_3P_3$ anode with exceptional Li storage performance, Energy Storage Mater. 36 (2021) 229–241.

[58] M. Nazarian-Samani, M. Nazarian-Samani, S. Haghighat-Shishavan, K.-B. Kim, Predelithiation-driven ultrastable Na-ion battery performance using Si, P-rich ternary M-Si-P anodes, Energy Storage Mater. 49 (2022) 421–432.

[59] R. Hu, D. Chen, G. Waller, Y. Ouyang, Y. Chen, B. Zhao, B. Rainwater, C. Yang, M. Zhu, M. Liu, Dramatically enhanced reversibility of Li_2O in SnO_2-based electrodes: The effect of nanostructure on high initial reversible capacity, Energ. Environ. Sci. 9 (2016) 595–603.

[60] M. Nazarian-Samani, A.R. Kamali, M. Nazarian-Samani, Study on solid state reactions of nanocrystalline Cu-Ge alloys upon mechanical alloying and annealing, Powder Metall. 57 (2014) 119–126.

[61] G. Zhang, Z.-W. Zhang, H.-J. Peng, J.-Q. Huang, Q. Zhang, A toolbox for lithium-sulfur battery research: Methods and protocols, Small Methods. 1 (2017) 1700134.

[62] H. Ye, J. Sun, X.F. Lim, Y. Zhao, J.Y. Lee, Mediator-assisted catalysis of polysulfide conversion for high-loading lithium–sulfur batteries operating under the lean electrolyte condition, Energy Storage Mater. 38 (2021) 338–343.

[63] J. Wang, L. Fan, Z. Liu, S. Chen, Q. Zhang, L. Wang, H. Yang, X. Yu, B. Lu, In situ alloying strategy for exceptional potassium ion batteries, ACS Nano 13 (2019) 3703–3713.

[64] K.-T. Chen, H.-Y. Tuan, Bi–Sb nanocrystals embedded in phosphorus as high-performance potassium ion battery electrodes, ACS Nano 14 (2020) 11648–11661.

[65] M. Nazarian-Samani, M. Nazarian-Samani, S. Haghighat-Shishavan, K.-B. Kim, Fe^{3+}-derived boosted charge transfer in an $FeSi_4P_4$ anode for ultradurable Li-ion batteries, ACS Nano 16 (2022) 12606–12619.

[66] X. Lan, J. Cui, X. Zhang, R. Hu, L. Tan, J. He, H. Zhang, X.Y. Xiong, X. Yang, S. Wu, M. Zhu, Boosting reversibility and stability of Li storage in SnO_2–Mo multilayers: Introduction of interfacial oxygen redistribution, Adv. Mater. 34 (2022) 2106366.

[67] S. Yang, C. Liu, H. Li, S. Wang, J. Choi, L. Li, Quantum dot heterostructure with directional charge transfer channels for high sodium storage, Energy Storage Mater. 39 (2021) 278–286.

[68] S.-K. Jung, I. Hwang, D. Chang, K.-Y. Park, S.-J. Kim, W.-M. Seong, D. Eum, J. Park, B. Kim, J. Kim, J.-H. Heo, K. Kang, Nanoscale phenomena in lithium-ion batteries, Chem. Rev. 120 (2020) 6684–6737.
[69] Y. Gogotsi, R.M. Penner, Energy storage in nanomaterials - capacitive, pseudocapacitive, or battery-like? ACS Nano 12 (2018) 2081–2083.
[70] S. Haghighat-Shishavan, M. Nazarian-Samani, M. Nazarian-Samani, H.-K. Roh, K.-Y. Chung, B.-W. Cho, S.F. Kashani-Bozorg, K.-B. Kim, Strong, persistent superficial oxidation-assisted chemical bonding of black phosphorus with multiwall carbon nanotubes for high-capacity ultradurable storage of lithium and sodium, J. Mater. Chem. A 6 (2018) 10121–10134.
[71] Y. Jin, N.-J.-H. Kneusels, L.E. Marbella, E. Castillo-Martínez, P.C.M.M. Magusin, R. S. Weatherup, E. Jónsson, T. Liu, S. Paul, C.P. Grey, Understanding fluoroethylene carbonate and vinylene carbonate based electrolytes for Si anodes in lithium ion batteries with NMR spectroscopy, J. Am. Chem. Soc. 140 (2018) 9854–9867.
[72] X. Yu, A. Manthiram, Electrode-electrolyte interfaces in lithium-based batteries, Energ. Environ. Sci. 11 (2018) 527–543.
[73] S. Haghighat-Shishavan, M. Nazarian-Samani, M. Nazarian-Samani, H.-K. Roh, K.-Y. Chung, S.-H. Oh, B.-W. Cho, S.F. Kashani-Bozorg, K.-B. Kim, Exceptionally reversible Li-/Na-ion storage and ultrastable solid-electrolyte interphase in layered GeP_5 anode, ACS Appl. Mater. Interfaces 11 (2019) 32815–32825.